

# Journal of Materials Chemistry A

Accepted Manuscript



This is an *Accepted Manuscript*, which has been through the Royal Society of Chemistry peer review process and has been accepted for publication.

*Accepted Manuscripts* are published online shortly after acceptance, before technical editing, formatting and proof reading. Using this free service, authors can make their results available to the community, in citable form, before we publish the edited article. We will replace this *Accepted Manuscript* with the edited and formatted *Advance Article* as soon as it is available.

You can find more information about *Accepted Manuscripts* in the [Information for Authors](#).

Please note that technical editing may introduce minor changes to the text and/or graphics, which may alter content. The journal's standard [Terms & Conditions](#) and the [Ethical guidelines](#) still apply. In no event shall the Royal Society of Chemistry be held responsible for any errors or omissions in this *Accepted Manuscript* or any consequences arising from the use of any information it contains.

Cite this: DOI: 10.1039/c0xx00000x

www.rsc.org/xxxxxx

ARTICLE TYPE

## Exploiting Stable Radical States for Multifunctional Properties in Triarylamine-based Porous Organic Polymers

Carol Hua,<sup>a</sup> Aditya Rawal,<sup>b</sup> Thomas B. Faust,<sup>a</sup> Peter D. Southon,<sup>a</sup> Ravichandar Babarao,<sup>c</sup> James M. Hook<sup>b</sup> and Deanna M. D'Alessandro<sup>\*a</sup>

Received (in XXX, XXX) Xth XXXXXXXXX 20XX, Accepted Xth XXXXXXXXX 20XX

DOI: 10.1039/b000000x

Redox-active porous organic polymers (POPs) have enormous potential in applications ranging from electrocatalysis to solar energy conversion. Exploiting the different electronic states offers exciting prospects for controlling host-guest chemistry, however, this aspect of multifunctionality has to date, remained largely unexplored. Here, we present a strategy for the development of multifunctional materials with industrially sought-after properties. A series of hydrophobic POPs containing redox-active triarylamines linked by ethynyl (POP-1), 1,4-diethynylphenyl (POP-2) and 4,4'-diethynylbiphenyl (POP-3) bridges have been synthesised and characterised by NMR and EPR spectroscopy, as well as spectroelectrochemistry and computational modelling. The facile electrochemical or chemical oxidation of the POPs generate mixed-valence radical cation states with markedly enhanced adsorption properties relative to their neutral analogues, including a 3-fold improvement in the H<sub>2</sub> uptake at 77 K and 1 bar, and an increase in the isosteric heat of adsorption for CO<sub>2</sub>.

### Introduction

Redox-active porous organic polymers (POPs) possess significant potential for interrogating fundamental aspects of electron delocalisation in 2- and 3-dimensional coordination space, while their potential to accommodate guest molecules within their structures paves the way towards applications in electrocatalysis, electrical swing adsorption, porous conductors and solar energy conversion devices, amongst others. To date, however, the interplay between host-guest properties and redox activity in POP materials has not been explored, despite the enormous potential to exploit the multifunctionality at both the fundamental and applied levels.

The triarylamine functionality represents an important structural motif in the quest for multifunctional redox-active POPs. In addition to the facile synthesis of the triarylamine core which allows the straightforward variation of substituents,<sup>1,2</sup> the distinctive redox and optical properties facilitate experimental and theoretical analyses of electron delocalisation.<sup>3</sup> In the latter case, the generation of the mixed-valence states of bridged triarylamines by chemical or electrochemical oxidation<sup>3,4</sup> and the appearance of characteristic optical bands known as Intervalence Charge Transfer (IVCT) transitions in the near-infrared region can provide powerful insights into the factors that govern the activation barriers to electron transfer.<sup>2</sup>

The oxidised radical cation and dication states of triarylamines have found applications as hole-transport components in photoconductors and light-emitting devices such as solar cells due to their electrical conductivity and electroluminescent

properties.<sup>5-7</sup> These properties have been exploited through the chemical and electrochemical synthesis of triarylamine-based polymers.<sup>8-14</sup> For example, oxidation of polytriarylamine systems *via* iodine doping has been employed as a strategy to enhance the electrical conductivity of these polymers up to 1 S cm<sup>-1</sup>.<sup>8</sup> Through electropolymerisation, electroactive thin films of triarylamine polymers have also been obtained by exploiting the unstable radical generated upon oxidation of non-*para* substituted triarylamine species.<sup>15-18</sup>

In contrast to the extensive literature concerning the electrochemical and optical properties of polytriarylamines, the interplay between their redox states and host-guest chemistry has not yet been explored, and limited studies have considered the porosity of porous organic networks derived from triarylamines. By comparison, the triarylamine functionality has been incorporated into a number of microporous metal-organic framework (MOF) systems, mainly as a structural motif with pyridyl<sup>19-21</sup> and carboxylate<sup>22-24</sup> terminated ligands. In the latter case, the frameworks are reported to have high surface areas, pore volumes and gas uptake, however, the potential redox activity has seldom been explored.<sup>25-30</sup>

The work presented herein provides a systematic exploration into the potential for exploiting different electronic states in triarylamine-based POPs to generate new multifunctional properties. The stable radical cation states of the triarylamine core, and hence, mixed-valence states of the polymers were exploited to quantify the extent of electronic delocalisation via analysis of the IVCT transitions in three POPs incorporating linkers of varying length, namely ethynyl (POP-1), 1,4-

diethynylphenyl (POP-2) and 4,4'-diethynyldiphenyl (POP-3). The redox and optical properties of two discrete model compounds, M1 and M2 containing the ethynyl and 1,4-diethynylphenyl linkers, respectively, provided a point of comparison with the POP solids. The molecular structures, synthesis methods and characterizations of these compounds are provided in the ESI.

The multifunctional properties of POP-2 and its radical analogue, POP-2a were exploited to address two applications of particular industrial importance, namely in H<sub>2</sub> storage<sup>31</sup> and CO<sub>2</sub> separation from flue gas streams.<sup>32,33</sup> Density Functional Theory (DFT) calculations were employed to provide insight on the origins of the differences in gas adsorption properties of POP-2 in its neutral and radical anion states. Despite the amorphous nature of the POPs,<sup>34</sup> they display a number of highly advantageous properties that underscore their enormous potential for industrial gas storage,<sup>35</sup> separation<sup>36</sup> and catalysis.<sup>37,38</sup> In particular, they are well known to exhibit improved chemical stabilities<sup>39</sup> relative to other 3-dimensional adsorbents such as MOFs, in which water can deactivate the active sites and/or decompose the materials. In the present work, the exploitation of stable radical states in triarylamine-based POPs provides a strategy towards the development of materials with highly sought-after multifunctional properties.

## Results and Discussion

### Synthesis and characterisation

The POPs were synthesised via a Sonogashira-Hagihara palladium cross coupling reaction between tris(*p*-ethynylphenyl)amine and tris(*p*-bromophenyl)amine, 1,4-dibromobenzene or 4,4'-dibromodiphenyl in the presence of Pd(PPh<sub>3</sub>)<sub>4</sub> and CuI as catalysts to form the respective polymers POP-1 (ethynyl linker), POP-2 (1,4-diethynylphenyl) and POP-3 (4,4'-diethynyldiphenyl) (Figure 1). Mono-coupling of the alkyne units and catalyst deactivation were minimised by conducting the syntheses under a nitrogen atmosphere. In all cases, the reaction mixture darkened from pale yellow to dark red/brown with subsequent formation of a yellow precipitate. Thermal gravimetric analysis indicated that all polymers displayed a high degree of thermal stability with decomposition occurring above 240 °C (ESI). The infrared spectrum of the monomer exhibits strong ν<sub>C≡H</sub> peaks at 3268 and 3279 cm<sup>-1</sup>, which disappear upon polymerisation (ESI). The ν<sub>C≡C</sub> is observed to shift from 2102 cm<sup>-1</sup> in the monomer to 2085 cm<sup>-1</sup> in the polymers.<sup>10</sup>

Further structural elucidation of the POPs was achieved through solid state NMR experiments (Figure 2). The <sup>13</sup>C CPMAS spectra of the polymers display one broad peak at 91.0

ppm due to the quaternary alkyne carbons; this peak was shifted upfield relative to the alkyne carbons in the tris(*p*-alkynylphenyl)amine monomer. The three peaks observed for the alkyne carbons in the starting material are indicative of different orientations of phenyl ring with respect to the packing of the molecule, resulting in different magnetic environments due to shielding and ring current effects from other tris(*p*-alkynylphenyl)amine molecules (Figure 2).

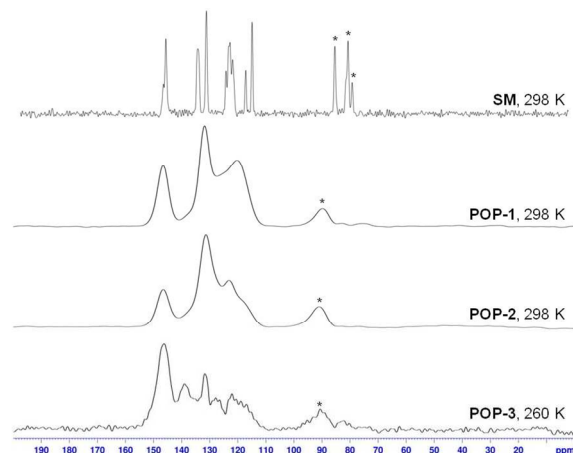


Figure 2. 75 MHz solid-state <sup>13</sup>C CPMAS NMR spectra at 8 kHz MAS with TOSS scheme, of the tris(*p*-alkynylphenyl)amine monomer (SM) and the POPs, where \* indicates the peak due to the alkyne carbons.

The identity of the alkyne carbons and other quaternary carbons in the POPs were further confirmed from the <sup>13</sup>C CP non-quaternary suppression (NQS) spectra (ESI) which only display signals due to carbons without hydrogen atoms directly attached. In each case, the peaks present in the <sup>13</sup>C CP NQS spectra were sharper and more highly resolved than those in the <sup>13</sup>C CPMAS spectra, indicating that the motional induced interference of decoupling due to the *sp*<sup>2</sup> carbons present in the POPs is reduced (as there are no *sp* carbons). The broadness of the spectra obtained for the polymers, where the peak at ~146 ppm has a linewidth at half height of ~380 Hz, is indicative of their amorphous nature when compared to the sharp peaks obtained for the monomeric tris(*p*-alkynylphenyl)amine starting material, where the peak at 147 ppm has a linewidth at half height of 54.0 Hz (ESI).

The broadness in the peaks due to the *sp*<sup>2</sup> carbons in the polymer is indicative of a correlation time that is on a timescale (millisecond) similar to that of the NMR experiment. This is likely to result from the phenyl rings between triarylamine cores being in motion and rotating around the axis. A similar observation was made for the broad peaks in the <sup>13</sup>C CPMAS spectrum of 1,4-dibromobenzene where the peaks remained broad

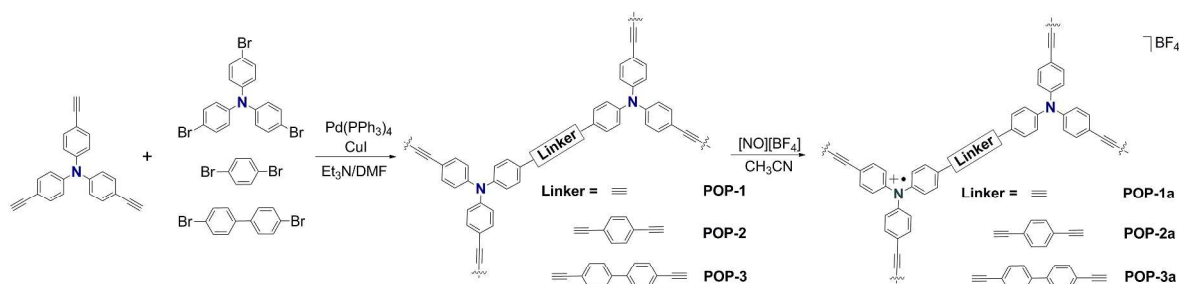


Figure 1. Synthetic scheme for the POPs and their oxidised analogues.

and poorly resolved, with a linewidth at half height of 550 Hz, even upon cooling to 260 K (ESI).

The fluxional movement of the phenyl linker groups may have consequences for electron delocalization, as maximum overlap of the  $\pi$  orbitals present in the alkynyl and phenyl moieties is required for effective electron transfer. The overlap of the  $\pi$  systems present would be maximised if a planar arrangement of the linker was achieved, or if these systems were rigid.<sup>40</sup>

### Redox Properties

The electrochemical properties of two discrete model compounds, M1 and M2 containing the ethynyl and 1,4-diethynylphenyl linkers, respectively, were investigated in the solution state in order to rationalise the redox processes in the corresponding POP solids (ESI). Cyclic voltammetry experiments were performed in [(n-C<sub>4</sub>H<sub>9</sub>)<sub>4</sub>N]PF<sub>6</sub>/CH<sub>3</sub>CN electrolyte and potentials are reported relative to the Fc/Fc<sup>+</sup> couple for both solution and solid state experiments.

Both discrete complexes exhibited two reversible redox processes in the anodic region between 0 and 1.0 V (at 0.084 and 0.58 V for M1 vs. 0.39 and 0.62 V for M2) which were assigned to formation of the radical cation and dication states, respectively, in agreement with previous literature reports (ESI).<sup>3</sup> At a potential intermediate to these two processes, the systems are in a mixed-valence state, where the odd electron is partially delocalised between the triarylamine cores.<sup>3</sup> The relatively higher separation between these two processes in M1 (0.50 V vs. 0.23 V for M2) suggests that the mixed-valence state is relatively more stable, as expected from the shorter N-N distance between the two triarylamine centres (9.93 Å in M1 versus 19.3 Å in M2) (ESI).<sup>3</sup>

The solid state cyclic voltammograms of POP-1 and POP-3 display broad quasi-reversible processes at *ca.* 0.75 and 0.95 V, respectively, that can be attributed to oxidation of the triarylamine core by analogy with M1 (ESI). For POP-1, the oxidation processes are quasi-reversible at a scan rate of 100 mV/s, and irreversible at a faster scan rate of 1000 mV/s, potentially due to slow diffusion of the counterions into the pores of the polymer. The broadness of the peaks indicates that formation of the monoradical cation and dication states may occur concurrently. By comparison, the cyclic voltammogram of POP-2 displays two well-defined redox processes at 0.45 and 0.95 V at a scan rate of 1000 mV/s (ESI). The enhancement in the reversibility of these processes with scan rate may reflect the more efficient diffusion of the counterions into the pores of POP-2 due to the higher surface area present relative to POP-1 (*vide infra*). Solid state spectroelectrochemical measurements on the POPs, including comparisons with their molecular analogues, enabled further insights into the origins of the redox processes.

### Optical Properties

The UV/Vis/NIR spectra of the polymers feature an intense, broad band above 20000 cm<sup>-1</sup>, which can be attributed to the  $\pi$  to  $\pi^*$  transition of the triarylamine core (ESI) and corresponds closely to the UV/Vis/NIR spectrum of the tris(*p*-alkynylphenyl)amine monomer. Vis/NIR solid state spectroelectrochemistry was performed on all three polymers in [(n-C<sub>4</sub>H<sub>9</sub>)<sub>4</sub>N]PF<sub>6</sub>/CH<sub>3</sub>CN electrolyte at potentials suitable for oxidation of the triarylamine moieties. The spectral progressions

accompanying one-electron oxidation of M1 and M2 to their mixed-valence states is provided for comparison (Figure 3a and 60 ESI) with the spectroelectrochemical data for the POPs.

Oxidation of the POPs was accompanied by the appearance of a band at ~ 12500 cm<sup>-1</sup> which was consistent with the formation of the radical cation of the triarylamine core (Figure 3b and ESI).<sup>1</sup> In all cases, the redox reactions appeared spectrally reversible when the potential was reduced to 0 V. All polymers exhibited a marked colour change from yellow to dark green/brown upon oxidation which was reversible upon reduction to the neutral species (ESI).

Of particular interest for the series of POPs was the relative degree of electron delocalisation as a function of linker length and the potential for mixed-valence behaviour, akin to that observed in linked triarylamine of the type exemplified in model compounds M1 and M2. The increase in the energy of the band ascribed to the triarylamine radical core from 11000 cm<sup>-1</sup> in POP-3 to 11500 and 13300 cm<sup>-1</sup> for POP-2, and POP-1, respectively, suggests that electron delocalisation in the systems increases as the distance between the triarylamine centers is reduced (Figure 3b and ESI). This effect is likely to arise from increased stabilisation of the more delocalised systems, resulting in a lower energy ground state and correspondingly, a higher energy transition to the excited state.<sup>3</sup> The band at ~22500 cm<sup>-1</sup>, which is attributed to the  $\pi$  to  $\pi^*$  transition of the triarylamine cores in the polymers exhibits a red shift and decrease in intensity upon oxidation, as shown for POP-1 in Figure 3b (and for POP-2 and 3 in the ESI).

Comparison of the spectroelectrochemical progression for M1 (Figure 3a) with that for POP-1 (Figure 3b), reveals the presence of a broad band in the NIR region at 6248 cm<sup>-1</sup> ( $\epsilon = 1297 \text{ M}^{-1}\text{cm}^{-1}$ ,  $\Delta\nu_{1/2} = 2242 \text{ cm}^{-1}$ ) for M1 and at 6377 cm<sup>-1</sup> ( $\Delta\nu_{1/2} = 3835 \text{ cm}^{-1}$ ) for POP-1. In both cases, the intensity of this band increases until it reaches a maximum, and then decreases. Corresponding data for model compound M2, and POP-2 and 3 are shown in the ESI. Interestingly, a broad band in the NIR is observed in M2 at 7800 cm<sup>-1</sup> ( $\epsilon = 1010 \text{ M}^{-1}\text{cm}^{-1}$ ,  $\Delta\nu_{1/2} = 4293 \text{ cm}^{-1}$ ), however no corresponding band was observed in POP-2 upon oxidation. The NIR region for POP-3 was also featureless upon oxidation. For POP-1, the observation of this NIR band is consistent with intramolecular electron transfer between the formally neutral and radical cation centers, as previously observed in linked triarylamine systems such as M1. By contrast, this coupling is negligible in POP-2 (despite the appearance of a weak IVCT band in M2) and POP-3.

The observation of an IVCT band in POP-1 is significant as it represents a low energy pathway for intramolecular electronic communication between the triarylamine centers. The NIR band in POP-1 is broader and occurs at a higher energy than that reported for M1 and the analogous dimer system in the literature<sup>3</sup> which is consistent with previous literature reports for electropolymerised triarylamine films.<sup>9</sup> Since measurements of the spectral intensities are challenging from these reflectance spectra, a related criterion for assessing delocalisation based on the experimental and predicted IVCT bandwidths may be employed according to equation (1),<sup>41</sup> where  $\Delta\nu_{1/2}^{\circ}$  is the theoretical bandwidth determined from Hush theory (ESI).<sup>42,43</sup>

$$\Gamma = 1 - (\Delta\nu_{1/2}) / (\Delta\nu_{1/2}^{\circ}) \quad (1)$$

The magnitude of the  $\Gamma$  parameter distinguishes the extent of delocalisation and class<sup>44</sup> of a mixed-valence system:  $0 < \Gamma < 0.1$  for weakly-coupled Class II systems,  $0.1 < \Gamma < 0.5$  for moderately-coupled localised Class II systems,  $\Gamma \approx 0.5$  at the localised-delocalised transition between Classes II and III, and  $\Gamma > 0.5$  for delocalised Class III systems. Based on the best fit Gaussian deconvolution to the NIR manifold in M1 and POP-1, the  $\Gamma$  values of 0.41 ( $\Delta\nu_{1/2} = 3799 \text{ cm}^{-1}$ ) and 0.042 ( $\Delta\nu_{1/2} = 3837 \text{ cm}^{-1}$ ), respectively, suggest that M1 exhibits relatively greater electronic delocalisation, approaching the localised-delocalised transition, while POP-1a exhibits approximately one tenth the degree of electronic delocalisation, consistent with a localized description.<sup>45</sup>

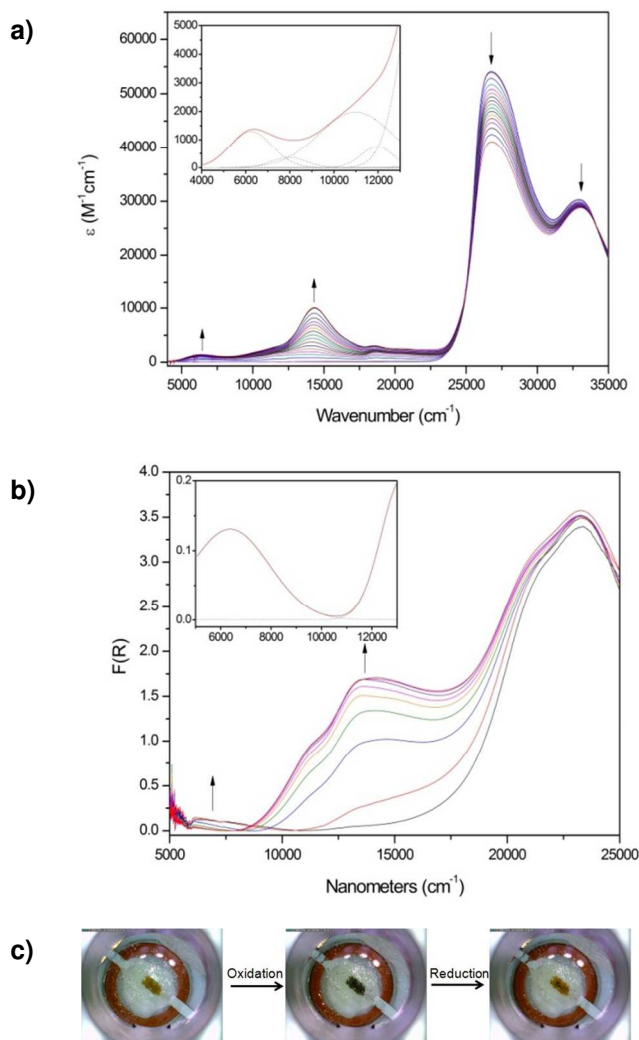


Figure 3. Spectroelectrochemistry on (a) model compound 1 (M1) showing oxidation to the mixed-valence radical cation state and (b) POP-1 showing oxidation to the radical cation state. The insets show the deconvolution and Gaussian curvefit to the near-IR band. (c) Photographs of POP-1 through the transparent working electrode during the spectroelectrochemical experiment.

The aforementioned results suggest that the appearance of IVCT bands in discrete organic mixed-valence systems provide insights into the mixed-valence properties of related polymeric systems. Electronic delocalisation in the polymers is enhanced upon generation of the mixed-valence state, however, the degree

of delocalisation diminishes as the distance between the multiply-linked redox-active moieties increases.

### Generation of the Radical POPs

Chemical oxidation of the polymers was achieved by the addition of a saturated solution of  $\text{NOBF}_4$  in dry acetonitrile to a suspension of the polymers in acetonitrile to yield POP-1a, 2a and 3a (Figure 1). The suspension was continuously purged with a stream of nitrogen to remove the liberated NO and prevent nitration of the aromatic moieties. For all polymers, a marked colour change in the solids was observed from yellow to green and finally to a dark brown upon addition of the oxidant (consistent with that observed using spectroelectrochemistry, Figure 3c). The thermal stability of the oxidised polymers is less than that of the neutral polymers, particularly for POP-1a (ESI).

The polymers can be oxidised to varying extents by altering the amount of oxidant added (ESI). The solid state UV/Vis/NIR spectra for the oxidised polymers revealed an increase in the band at  $\sim 11000 \text{ cm}^{-1}$  with increasing amounts of oxidation and a decrease in the broad band above  $30000 \text{ cm}^{-1}$ . A red shift of the shoulder band at  $\sim 22000 \text{ cm}^{-1}$  to  $\sim 20500 \text{ cm}^{-1}$  was also observed. The band at  $\sim 11000 \text{ cm}^{-1}$  is consistent with that observed in the spectroelectrochemical measurements and is characteristic of the  $D_0$  to  $D_1$  transition previously reported for the triarylamine core.<sup>1</sup> The integrity of the alkynyl bond during the oxidation process was established by inference from an *in situ* NMR study on M1 in dichloromethane at  $25^\circ \text{C}$  (ESI). The  $^{13}\text{C}\{^1\text{H}\}$  NMR spectrum obtained after one day showed the appearance of a peak at 87.6 ppm and confirmed the stability of the alkynyl bond to  $\text{NOBF}_4$  (ESI).

The extent of oxidation in the chemically-oxidised polymers was estimated by comparing the ratio of the intensity of the bands at  $\sim 12500 \text{ cm}^{-1}$  and  $22500 \text{ cm}^{-1}$  in the neutral and oxidised systems. This comparison revealed that the extent of oxidation of the polymers using  $\text{NOBF}_4$  was  $< 5\%$ , suggesting the presence of a low concentration of radical centers.

The high dilution of radicals was confirmed by solid state EPR and NMR experiments. The EPR spectra of the oxidised POPs all exhibited a large increase in signal intensity compared with their non-oxidised analogues together with the hyperfine structure from coupling with the  $^{14}\text{N}$  nucleus ( $I = 1$ ), which was observed for the parallel axis only. Since hyperfine anisotropy along the perpendicular axes is small, the hyperfine components along these axes are likely to be poorly resolved and likely sum to give the large central feature. The anisotropic hyperfine parameter,  $2A_{\parallel}$ , is slightly lower for POP-1a (33.4 gauss) than for POP-2a and -3a (37.3 and 36.7 gauss respectively; see Figure 4 and ESI). Any additional hyperfine coupling from the protons is poorly resolved and is likely to contribute to some of the line broadening, as is any small  $g$ -anisotropy which cannot be elucidated at this frequency. The presence of hyperfine structure confirms that, following oxidation with  $\text{NOBF}_4$ , the radicals still exist in high dilution within the polymer.  $g$ -Values for all samples are approximately 2.006, higher than that of the triphenylamine radical (2.003)<sup>46</sup> and the bis(triarylamine) monocations reported by Barlow (2.004).<sup>47</sup>

NMR measurements of the relaxation times of the oxidised polymer provided additional insight into the extent of delocalisation in the polymers. Since a paramagnetic radical

provides a mechanism for both the  $T_1$  and  $T_2$  modes of relaxation for any particular nuclei, the presence of radicals in high concentrations leads to very short relaxation times (in the order of 100 ms) for nuclei interacting with the delocalised electron. In the present case, the  $T_1$  relaxation times for  $^1\text{H}$  species in POP-2 were in the order of 3-10 seconds (Table S2 in ESI), which is typical for an amorphous solid containing a dilute concentration of localized radical centers (ESI).

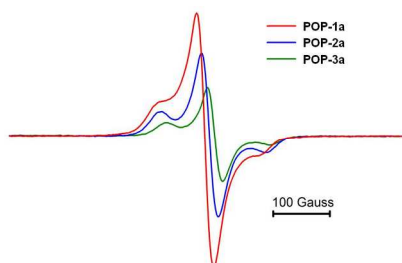


Figure 4. X-band solid state EPR spectra at 298 K for POP-1a, -2a and -3a.

### Gas Adsorption

The porosity of the POPs was examined through measurement of the BET surface areas for the polymers which were determined as 510, 781 and 752  $\text{m}^2/\text{g}$  for POP-1, POP-2 and POP-3, respectively (Figure 5a). The highest surface area was observed for POP-2, suggesting that the surface areas are a function of not only the linker length, but also the degree of interpenetration. A large hysteresis was observed in the nitrogen isotherm at 77 K for all of the POPs, which can be attributed to a degree of flexibility in the polymer systems (Figure 5a). The step in the  $\text{N}_2$  desorption isotherm for POP-3 at *ca.* 500 mbar may be indicative of the presence of mesopores, or significant structural movement of the interpenetrated polymer networks. The predominant pore diameter for all POPs was  $\sim 6$  Å, with larger pores of 10 and 12.5 Å diameter also identified (ESI). POP-2 and its oxidised analogue, POP-2a were selected for subsequent gas adsorption experiments in view of its maximal surface area of the series.

Three fundamental material properties of particular relevance to the capture of  $\text{CO}_2$  from flue gas are the uptake capacity, selectivity over other components in the flue stream (particularly  $\text{N}_2$  and  $\text{H}_2\text{O}$ ) and the isosteric heat of adsorption,  $-Q_{\text{st}}$ , at industrially relevant pressures and temperatures (typically evaluated at 0.15 bar and 298 K).<sup>32-33</sup> The  $\text{N}_2$  isotherm at 77 K (Figure 5a) indicated that the surface area for the oxidized POP-2a (440  $\text{m}^2/\text{g}$ ) was significantly lower than that of POP-2 (781  $\text{m}^2/\text{g}$ ) due to the presence of the  $\text{BF}_4^-$  counterions in the pores of the oxidised polymer. Despite the reduced surface area of POP-2a relative to its neutral analogue, the  $\text{CO}_2$  uptake at 0.15 bar was marginally improved (0.342 mmol/g versus 0.302 mmol/g for POP-2), while  $-Q_{\text{st}}$  was significantly enhanced (27 kJ/mol versus 17 kJ/mol for POP-2 at zero coverage) (Figure 5b). The relative magnitudes of  $-Q_{\text{st}}$  indicate that  $\text{CO}_2$  exhibits a relatively stronger affinity for POP-2a relative to its neutral analogue. The introduction of charges to the polymer allows for increased electrostatic interactions with the quadrupolar  $\text{CO}_2$  molecules. In the case of the neutral material, the  $-Q_{\text{st}}$  of 17 kJ/mol is comparable to the enthalpy of liquefaction of  $\text{CO}_2$ , indicating that the affinity of the gas for itself is comparable to its affinity for the

material. The uptake of  $\text{CO}_2$  in POP-2 and POP-2a is moderate when compared to other porous solids such as Metal-Organic Frameworks (MOFs) and carbonaceous materials.<sup>32,48</sup>

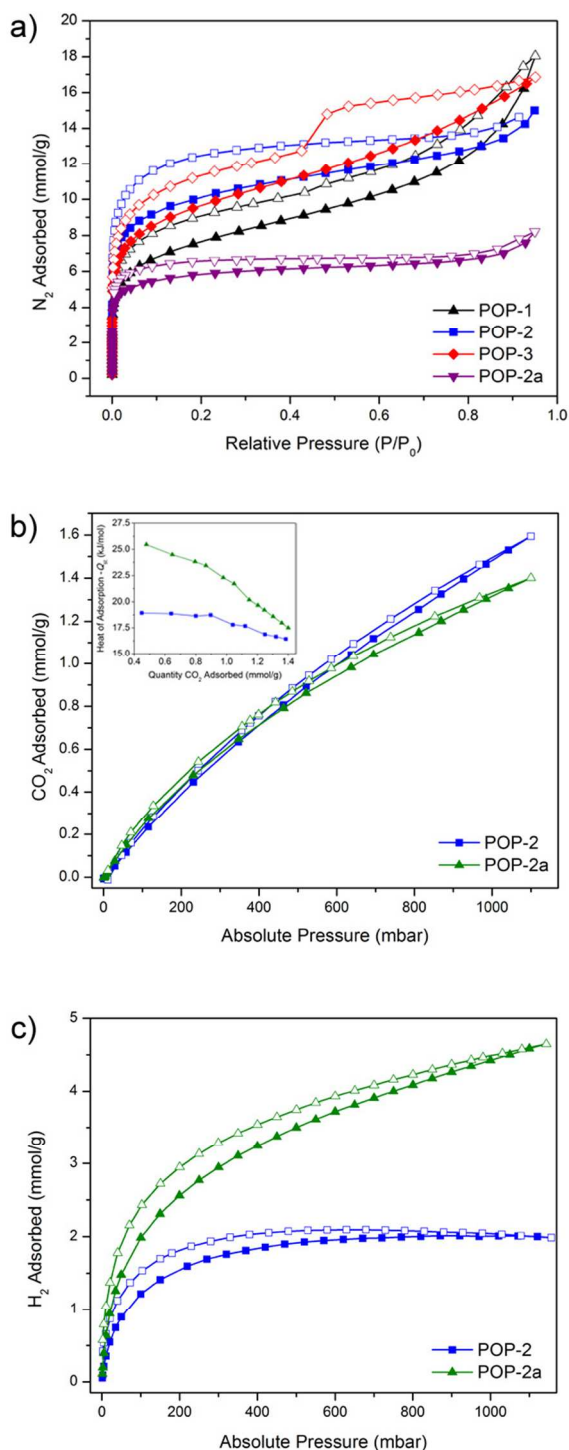


Figure 5. Gas adsorption over the 0-1000 mbar pressure region where a)  $\text{N}_2$  isotherms for all POPs at 77 K, b)  $\text{CO}_2$  isotherms for POP-2 and POP-2a at 298 K with heat of adsorption for  $\text{CO}_2$  (inset) and c)  $\text{H}_2$  isotherms for POP-2 and POP-2a at 77 K.

Gas adsorption measurements over the 0-10 bar pressure range for  $\text{CO}_2$  and  $\text{N}_2$  at 298 K revealed selective adsorption for  $\text{CO}_2$  over  $\text{N}_2$  in POP-2 (Figure 6a). In addition, a water adsorption

isotherm revealed that POP-2 is hydrophobic – a property that is highly advantageous if such materials are to be applied in the separation of CO<sub>2</sub> from gas flue streams which contain up to 10 mol% H<sub>2</sub>O (Figure 6b).<sup>32,33</sup>

5 Remarkably, the H<sub>2</sub> uptake exhibits a 3-fold enhancement at 77 K and 1 bar (Figure 5c), despite the reduced surface area of POP-2a relative to its neutral analogue, demonstrating the significant potential of exploiting stable radical states in POP solids to enhance gas storage.

10 DFT calculations were pursued to gain insight into the optimised locations of CO<sub>2</sub> and H<sub>2</sub> in a model fragment of POP-2 and POP-2a incorporating a BF<sub>4</sub><sup>-</sup> counterion (ESI). An increase in the static binding energies was predicted for CO<sub>2</sub> and H<sub>2</sub> adsorption in the oxidised system (-16.4 versus -23.4 kJ/mol for CO<sub>2</sub> in POP-2 and 2a, respectively; -4.8 versus -12.7 kJ/mol for H<sub>2</sub> in POP-2 and -2a, respectively), supporting the presence of increased electrostatic interactions between the gas molecules and the oxidised framework. The origin of the enhancement is primarily attributed to interactions between the CO<sub>2</sub> or H<sub>2</sub> molecules and the BF<sub>4</sub><sup>-</sup> anions which are located in close proximity to the triarylamine radical centers of the model fragments. Indeed, previous literature reports have noted increased gas uptakes due to the interaction of CO<sub>2</sub> with anions such as PF<sub>6</sub><sup>-</sup> present in the pores of MOFs.<sup>49</sup>

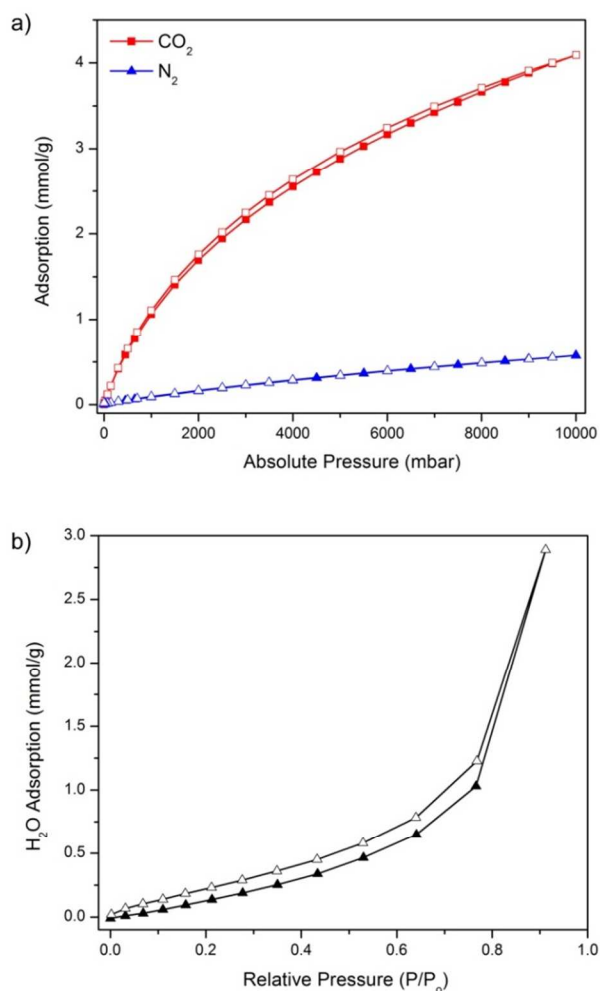


Figure 6. Gas and vapor adsorption over the 0-10000 mbar pressure region in POP-2 at 298 K where a) N<sub>2</sub> and CO<sub>2</sub> isotherms and b) H<sub>2</sub>O isotherm (adsorption = filled symbols, desorption = open symbols).

## Conclusions

30 Redox-active porous organic polymer networks possess significant potential for interrogating fundamental aspects of electron delocalisation in 2- and 3-dimensional coordination space, while their multifunctional properties pave the way towards applications which exploit the porosity for host-guest chemistry. In the present work, coupling the adsorption properties with redox activity leads to enhanced adsorption of H<sub>2</sub> and an enhanced isosteric heat of adsorption for CO<sub>2</sub> in the oxidised POPs which incorporate triarylamine radical cation centers. The ability to reversibly generate the neutral and radical states *via* electrochemical and spectroelectrochemical measurements suggest that these materials may prove valuable in the development of electrical swing adsorption methods for the capture and release of CO<sub>2</sub>. Importantly, their hydrophobicity surmounts one of the common drawbacks of other microporous materials such as MOFs for industrial flue gas capture, namely the deactivation of the adsorption sites due to water binding.

The present work also demonstrates that *in situ* spectroelectrochemical analysis of the IVCT transitions offers a window to the mixed-valence character of redox-active solids. The observation of weak electronic delocalisation between the redox-active triarylamine units in the mixed-valence forms of the POPs, reveals that the intercomponent interactions can be modulated by varying the bridging linker. Importantly, enhancing the extent of electronic delocalisation in these amorphous materials and their semi-crystalline covalent organic framework (COF) analogues should lead the way towards highly sought-after conducting microporous materials.<sup>50</sup>

## Experimental

All chemicals and solvents were used as obtained and used without further purification. Acetonitrile and triethylamine were dried over CaH<sub>2</sub> and dimethylformamide dried over activated CaSO<sub>4</sub>. A detailed account of the synthetic procedures for ligands is provided in the ESI.

**Synthesis of POPs.** Tris(*p*-ethynylphenyl)amine (0.200 g, 0.625 mmol), the linker (0.500 mmol) and Pd(PPh<sub>3</sub>)<sub>4</sub> (7.5 mg, 6.49 x 10<sup>-6</sup> mol) were dissolved in a mixture of dry and degassed triethylamine (3.0 mL) and dimethylformamide (3.0 mL). The reaction mixture was stirred under nitrogen at room temperature for 5 minutes prior to the addition of copper iodide (2.5 mg, 1.31 x 10<sup>-6</sup> mol). The reaction mixture was heated to 75 °C upon which a yellow solid rapidly formed. The mixture was heated for a further 15 minutes before being cooled and filtered. The bright yellow solid was washed successively with DMF, chloroform, methanol, water, methanol and acetone to ensure complete removal of unreacted starting material, catalyst and triethylamine solvent molecules, before being washed in a soxhlet extraction with methanol overnight to ensure complete removal of DMF. The yellow solid was then dried to yield the product. POP-1: Yield = 250 mg, UV-Vis-NIR (solid state): 23340, 31609, 41975 cm<sup>-1</sup>, Elemental Analysis: Found C, 72.61; H, 4.43 and N, 5.67. POP-2: Yield = 275 mg, UV-Vis-NIR (solid state): 24123, 30837,

34419, 42687  $\text{cm}^{-1}$ , Elemental Analysis: Found C, 83.10; H, 6.62 and N, 3.42. POP-3: Yield = 218 mg, UV-Vis-NIR (solid state): 23602, 30766, 34549, 41975  $\text{cm}^{-1}$ , Elemental Analysis: Found C, 80.88; H, 4.61 and N, 3.38.

5 **Oxidation of POPs.** The POP (20 mg) was suspended in dry and distilled acetonitrile (2 mL) and the mixture thoroughly degassed. A solution of nitrosium tetrafluoroborate (10 mg, 0.0860 mmol) in acetonitrile (2 mL) was added slowly dropwise with vigorous bubbling of nitrogen to yield an immediate colour change from  
10 yellow to dark brown. The mixture was left to stir at room temperature with vigorous bubbling of nitrogen for 30 minutes, the solid filtered off and dried. POP-1a: UV-Vis-NIR (solid state): 11680, 14350, 21640, 31680, 41774  $\text{cm}^{-1}$ , Elemental Analysis: Found C, 49.37; H, 4.02 and N, 7.47. POP-2a: UV-Vis-  
15 NIR (solid state): 11490, 22890, 32000, 42356  $\text{cm}^{-1}$ , Elemental Analysis: Found C, 70.80; H, 4.50 and N, 5.09. POP-3a: UV-Vis-NIR (solid state): 11811, 23080, 34218, 42878  $\text{cm}^{-1}$ , Elemental Analysis: Found C, 56.78; H, 3.31 and N, 5.54.

### Physical Properties and Instrumentation

20 **Solid State NMR.** The  $^{13}\text{C}$  CPMAS solid state NMR experiments were carried out on a wide-bore Bruker Biospin Avance III solids-300 MHz spectrometer operating at a frequency of 75 MHz for the  $^{13}\text{C}$  nucleus and 300 MHz for the  $^1\text{H}$  nucleus. Approximately 80 mg of samples were into 4 mm zirconia rotors  
25 fitted with Kel-f<sup>®</sup> caps and spun in a double resonance H-X probehead at 8 kHz MAS (magic angle spinning). The  $^{13}\text{C}$  and  $^1\text{H}$  90° radio frequency pulse lengths were optimised to 3.5  $\mu\text{s}$  each. The  $^{13}\text{C}$  spectra were acquired with 1 ms cross polarization contact time with a total suppression of spinning sidebands  
30 (TOSS) scheme, followed by  $^1\text{H}$  decoupling at 75 kHz field strength using spinal-64 decoupling. The  $^{13}\text{C}$  NQS (non-quaternary carbon suppression) spectra were recorded by turning off the  $^1\text{H}$  decoupling for 40  $\mu\text{s}$  during the TOSS period. For sufficient signal to noise, ca. 10 k transient were acquired for  
35 each sample with recycle delays of 3.0 in between to ensure sufficient relaxation of the  $^1\text{H}$  nuclei. While the spectra for the POP-1 and POP-2 were at room temperature, the spectra for POP-3 were collected at 260 K. The  $^{13}\text{C}$  chemical shifts were referenced to the glycine CO peak at 176 ppm. The  $^1\text{H}$ -T<sub>1</sub>  
40 relaxation experiments were measured using a saturation recovery pulse sequence on an Avance III 700 MHz standard bore spectrometer with 4 mm H-X double resonance probehead. The  $^1\text{H}$  90° pulse lengths were optimized to 3.25  $\mu\text{s}$  and the rotor was spun to 14 kHz MAS.

45 **Electrochemistry.** Solid state electrochemical measurements were performed using a Bioanalytical Systems BAS 100A Electrochemical Analyser. Argon was bubbled through solutions of 0.1 M [(*n*-C<sub>4</sub>H<sub>9</sub>)<sub>4</sub>N]PF<sub>6</sub> dissolved in distilled CH<sub>3</sub>CN. The cyclic voltammograms (CVs) were recorded using a glassy  
50 carbon working electrode (1.5 mm diameter), a platinum wire auxiliary electrode and an Ag/Ag<sup>+</sup> wire quasi reference electrode. Solid state samples were mounted on the glassy carbon working electrode by dipping the electrode into a paste made of the powder sample in acetonitrile. Ferrocene was added as an internal  
55 standard upon completion of each experiment. All potentials are quoted in mV versus Fc<sup>+</sup>/Fc<sup>0</sup>.

**UV/Vis/NIR.** UV/Vis/NIR spectroscopy was performed on a Cary 5E Spectrophotometer equipped with a Harrick Praying

Mantis accessory, where dried KBr was used for the baseline. Spectra are reported as the Kubelka-Munk transform F(R) as a function of wavenumber ( $\text{cm}^{-1}$ ).

**Spectroelectrochemistry.** Solution state UV/Vis/NIR spectroelectrochemistry over the range of 3500-35000  $\text{cm}^{-1}$  was performed using a CARY 5000 spectrophotometer interfaced to  
65 Varian WinUV software. In the solution state, the absorption spectra of the electrogenerated mixed-valence species were obtained *in situ* by the use of an Optically Semi-Transparent Thin-Layer Electrochemical (OSTLE) cell, path length 0.65 mm, mounted in the path of the spectrophotometer. Solutions for the  
70 spectroelectrochemical experiment contained 0.1 M [(*n*-C<sub>4</sub>H<sub>9</sub>)<sub>4</sub>N]PF<sub>6</sub>/dichloromethane (DCM) supporting electrolyte and ca. 1 mM of the compound. Appropriate potentials were applied by using an eDAQ e-corder 410 potentiostat and the current was carefully monitored throughout the electrolysis. By this method,  
75 the electrogenerated mixed-valence species (which are otherwise unstable) were obtained *in situ*, and their absorption spectra were recorded at regular intervals throughout the electrolysis. The attainment of a steady-state spectrum and the decay of the current to a constant minimum at a potential appropriately beyond E<sub>1/2</sub>  
80 (for the redox process in question) was indicative of the complete conversion of the starting material. For the mixed-valence species, a potential intermediate between the two metal-centered redox processes was employed. The reversibility of the spectral data was confirmed by the observation of stable isosbestic points,  
85 and the regeneration of the starting spectrum following the attainment of the steady-state spectrum for the mixed-valence species.

In the solid state, the diffuse reflectance spectra of the electrogenerated species were collected *in situ* in a 0.1 M [(*n*-C<sub>4</sub>H<sub>9</sub>)<sub>4</sub>N]PF<sub>6</sub>/CH<sub>3</sub>CN electrolyte over the range 5000-25000  $\text{cm}^{-1}$  using a Harrick Omni Diff Probe attachment and a custom built solid state spectroelectrochemical cell described previously.<sup>51</sup> The cell consisted of a Pt wire counter electrode and Ag/Ag<sup>+</sup> quasi reference electrode were used. The solid sample was  
95 immobilised onto an 0.1 mm thick Indium-Tin-Oxide (ITO) coated quartz slide (which acts as the working electrode) using a thin strip of Teflon tape followed by the addition of LiClO<sub>4</sub>-intercalated PVC (to a diameter of 1 cm). The applied potential (from 0.5 V to 3.0 V) was controlled using an eDAQ potentiostat.  
100 Continuous scans of the sample were taken and the potential increased gradually until change in the spectrum was observed.

**Electron Paramagnetic Resonance (EPR) spectroscopy.** EPR spectroscopy (Bruker EMX-X band) was performed at room temperature on freshly synthesised materials (~12 mg). The  
105 microwave frequency was between 9.75 and 9.85 GHz for all measurements and the microwave power well below that required for saturation. All other parameters remained constant: receiver gain,  $1 \times 10^5$ ; modulation frequency, 100 kHz; modulation amplitude, 1.00 G; sweep width, 400 G; resolution, 1024 point;  
110 conversion, 40.960 ms; time constant, 40.960 ms; sweep time, 41.943 s and each spectrum was averaged over four scans.

Note that oxidation *via* NOBF<sub>4</sub> results in the release of diatomic NO which normally reacts in air to produce NO<sub>2</sub>. The authors considered the possibility of NO/NO<sub>2</sub> physisorption  
115 within the internal cavities of framework as the stable paramagnetic di- and triatomics could present themselves as

spectral triplets (such an observation has been made before for NO<sub>x</sub> in zeolitic materials<sup>52</sup> and following superposition with a strong singlet arising from the triarylamine give a spectrum resembling that observed. To test this hypothesis oxidised samples were run as synthesised and then again following 5 degassing cycles. The results show that this was adequate to remove all native gases. The resultant spectra were not discernibly different from the as synthesised and so this theory was dismissed.

**10 Thermal gravimetric analysis (TGA).** TGA was performed under a flow of nitrogen (0.1 L/min) on a TA Instruments Hi-Res Thermogravimetric Analyser from 25-600 °C at 1 °C/min.

**Gas adsorption.** Gas adsorption measurements over the 0-1 bar range were conducted using a Micromeritics Accelerated Surface Area and Porosity (ASAP) 2020 instrument. Approximately 50-100 mg of the polymer sample was degassed under vacuum at 70 °C for approximately 14 hours. Nitrogen adsorption isotherms were measured at 77 K via the incremental dosing of nitrogen from 0-1 bar, and surface areas determined via the BET method using the ASAP2020 V4.01 software. CO<sub>2</sub> isotherms at 298 K, 308 K and 318 K were measured on the same instrument, with temperature controlled by a Julabo F25 Circulating Heating and Cooling bath. The enthalpy of adsorption for CO<sub>2</sub> was calculated using data from the three CO<sub>2</sub> isotherms and the Clausius-Clapeyron equation (see Figures S20-22 and Tables S4 and S5). An estimation of the porosity distribution in the POPs was obtained using the Tarazona Non-Local Density Functional Theory (with cylindrical pores) implemented within the Micromeritics ASAP 2020 software (Version 4.0).

Adsorption isotherms over the 0-10 bar range were measured with a Hiden-Isochema IGA-002 gravimetric system. The sample was loaded into a stainless steel mesh basket and evacuated under high vacuum at 70 °C for 15 hours, after which the sample mass was stable. The sample was maintained at 25 ± 0.1 °C during measurement of the isotherm. At each data point the pressure in the sample chamber was set and the mass allowed to equilibrate before moving to the next data point. The equilibrium mass was corrected for the buoyancy of the sample and balance components; the sample density was measured by a helium displacement isotherm to 10 bar. The water used to generate the water vapour was degassed fully by repeated evacuation of the vapour reservoir. The gasses used were supplied at 99.99% purity.

**Computational Calculations.** The static binding energies for CO<sub>2</sub> and H<sub>2</sub> at zero Kelvin were calculated using the dispersion-corrected semi-empirical DFT-D2 method.<sup>53</sup> All calculations were performed using Vienna *ab initio* simulation package (VASP)<sup>54,55</sup> with a plane-wave energy cut-off of 400 eV and a Gamma-point mesh for sampling the Brillouin zone. A detailed account of these methods is provided in the ESI.

**Acknowledgements.** We gratefully acknowledge support from the Australian Research Council and the Science and Industry Endowment Fund. We also thank Professor Mike Davies (Heart Research Institute, The University of Sydney) for the provision of EPR spectrometer access and Professor David Collison (The University of Manchester) for helpful discussions.

## Notes and references

<sup>a</sup> School of Chemistry, The University of Sydney, New South Wales 2006, Australia. Fax: +61 (2) 9351 3329; Tel: +61 (2) 9351 3777; E-mail:

deanna.dalessandro@sydney.edu.au

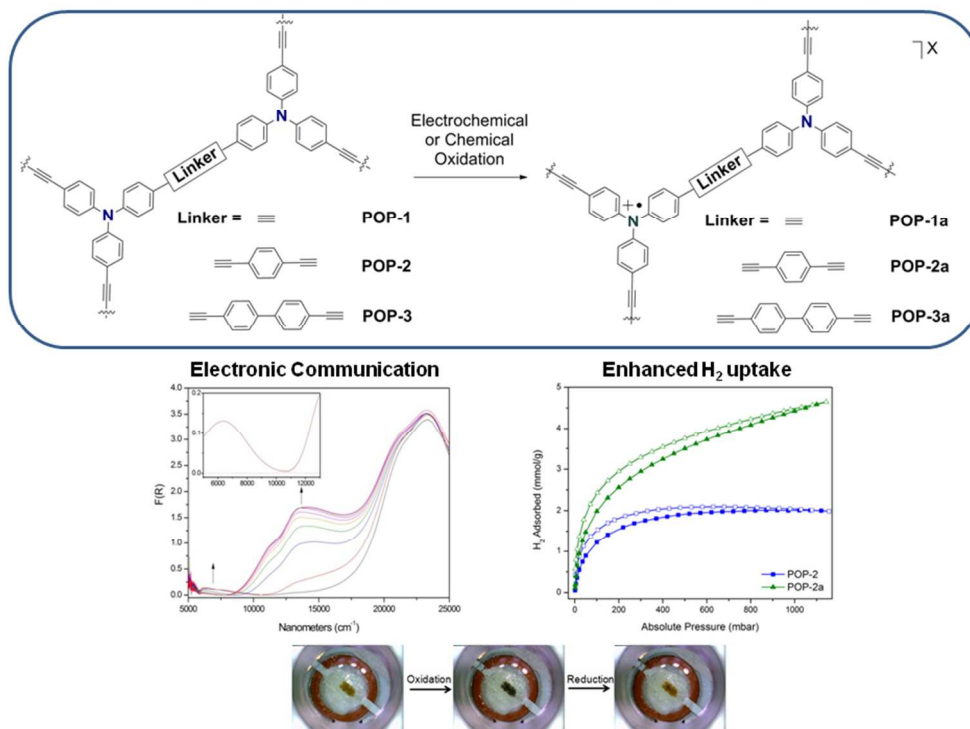
<sup>b</sup> NMR Facility, Mark Wainwright Analytical Centre, The University of New South Wales, New South Wales 2052, Australia

<sup>c</sup> Materials Science and Engineering Division, Commonwealth Scientific and Industrial Research Organisation (CSIRO), Clayton, Victoria 3168, Australia

† Electronic Supplementary Information (ESI) available: additional synthetic details, TGA, FTIR, NMR, electrochemical, spectral, spectroelectrochemical, adsorption and computational data. See DOI: 10.1039/b000000x/

1. S. Amthor, B. Noller, C. Lambert, *Chem. Phys.* 2005, **316**, 141-152.
2. A. Heckmann, C. Lambert, *Angew. Chem. Int. Ed.* 2012, **51**, 326-392.
3. C. Lambert, G. Nöll, *J. Am. Chem. Soc.* 1999, **121**, 8434-8442.
4. S. Amthor, C. Lambert, *J. Phys. Chem. A* 2005, **110**, 1177-1189.
5. B. Simone, A. Quartarolo, S. Cospito, L. Veltri, G. Chidichimo, N. Russo, *Theor. Chem. Acc.* 2012, **131**, 1-9.
6. H.-J. Yen, H.-Y. Lin, G.-S. Liou, *Chem. Mater.* 2011, **23**, 1874-1882.
7. H.-J. Yen, G.-S. Liou, *Polym. Chem.* 2012, **3**, 255-264.
8. M. Ishikawa, M. Kawai, Y. Ohsawa, *Synth. Met.* 1991, **40**, 231-238.
9. Y. Ohsawa, M. Ishikawa, T. Miyamoto, Y. Murofushi, M. Kawai, *Synth. Met.* 1987, **18**, 371-374.
10. S. W. Kim, S. C. Shim, D. Y. Kim, C. Y. Kim, *Synth. Met.* 2001, **122**, 363-368.
11. W. Shi, S. Fan, F. Huang, W. Yang, R. Liu, Y. Cao, *J. Mater. Chem.* 2006, **16**, 2387-2394.
12. F. E. Goodson, S. I. Hauck, J. F. Hartwig, *J. Am. Chem. Soc.* 1999, **121**, 7527-7539.
13. G. I. Nosova, A. V. Yakimanskii, N. A. Solovskaya, E. V. Zhukova, R. Y. Smyslov, A. R. Tameev, E. L. Aleksandrova, T. V. Magdesieva, *Polym. Sci. Ser. B* 2011, **53**, 16-25.
14. K. R. Prashanth Kumar, M. G. Murali, D. Udayakumar, *Des. Monomers Polym.* 2013, 1-12.
15. M. I. Mangione, R. A. Spanevello, A. Rumbero, D. Heredia, G. Marzari, L. Fernandez, L. Otero, F. Fungo, *Macromol.* 2013, **46**, 4754-4763.
16. T. Lana-Villarreal, J. M. Campiña, N. Guijarro, R. Gómez, *Phys. Chem. Chem. Phys.* 2011, **13**, 4013-4021.
17. A. Petr, C. Kvarnström, L. Dunsch, A. Ivaska, *Synth. Met.* 2000, **108**, 245-247.
18. C. Lambert, G. Nöll, *Synth. Met.* 2003, **139**, 57-62.
19. M.-D. Zhang, C.-M. Di, L. Qin, X.-Q. Yao, Y.-Z. Li, Z.-J. Guo, H.-G. Zheng, *Cryst. Growth Des.* 2012, **12**, 3957-3963.
20. M.-D. Zhang, L. Qin, H.-T. Yang, Y.-Z. Li, Z.-J. Guo, H.-G. Zheng, *Cryst. Growth Des.* 2013, **13**, 1961-1969.
21. C. Hua, D. M. D'Alessandro, *CrystEngComm* 2014, Advance Article, DOI: 10.1039/C3CE42603C.
22. C. Livage, N. Guillou, A. Castiglione, J. Marrot, M. Frigoli, F. Millange, *Micro. Meso. Mater.* 2012, **157**, 37-41.
23. C. Ding, X. Li, Y. Ding, X. Li, S. W. Ng, Y. Xie, *Cryst. Growth Des.* 2012, **12**, 3465-3473.
24. H. K. Chae, J. Kim, O. D. Friedrichs, M. O'Keeffe, O. M. Yaghi, *Angew. Chem. Int. Ed.* 2003, **42**, 3907-3909.
25. H. J. Park, D.-W. Lim, W. S. Yang, T.-R. Oh, M. P. Suh, *Chem. Eur. J.* 2011, **17**, 7251-7260.
26. E. Y. Lee, S. Y. Jang, M. P. Suh, *J. Am. Chem. Soc.* 2005, **127**, 6374-6381.
27. D. Shi, Y. Ren, H. Jiang, B. Cai, J. Lu, *Inorg. Chem.* 2012, **51**, 6498-6506.
28. H. J. Park, Y. E. Cheon, M. P. Suh, *Chem. Eur. J.* 2010, **16**, 11662-11669.
29. M. P. Suh, Y. E. Cheon, E. Y. Lee, *Chem. Eur. J.* 2007, **13**, 4208-4215.
30. Y. E. Cheon, M. P. Suh, *Angew. Chem. Int. Ed.* 2009, **48**, 2899-2903.
31. L. J. Murray, M. Dinca, J. R. Long, *Chem. Soc. Rev.* 2009, **38**, 1294-1314.
32. D. M. D'Alessandro, B. Smit, J. R. Long, *Angew. Chem. Int. Ed.* 2010, **49**, 6058-6082.

33. K. Sumida, D. L. Rogow, J. A. Mason, T. M. McDonald, E. D. Bloch, Z. R. Herm, T.-H. Bae, J. R. Long, *Chem. Rev.* 2011, **112**, 724-781.
34. D. Wu, F. Xu, B. Sun, R. Fu, H. He, K. Matyjaszewski, *Chem. Rev.* 2012, **112**, 3959-4015.
35. H. A. Patel, S. Hyun Je, J. Park, D. P. Chen, Y. Jung, C. T. Yavuz, A. Coskun, *Nat. Commun.* 2013, **4**, 1357.
36. O. K. Farha, A. M. Spokoyny, B. G. Hauser, Y.-S. Bae, S. E. Brown, R. Q. Snurr, C. A. Mirkin, J. T. Hupp, *Chem. Mater.* 2009, **21**, 3033-3035.
37. J.-X. Jiang, C. Wang, A. Laybourn, T. Hasell, R. Clowes, Y. Z. Khimiyak, J. Xiao, S. J. Higgins, D. J. Adams, A. I. Cooper, *Angew. Chem. Int. Ed.* 2011, **50**, 1072-1075.
38. K. Zhang, D. Kopetzki, P. H. Seeberger, M. Antonietti, F. Vilela, *Angew. Chem. Int. Ed.* 2013, **52**, 1432-1436.
39. T. Ben, H. Ren, S. Ma, D. Cao, J. Lan, X. Jing, W. Wang, J. Xu, F. Deng, J. M. Simmons, S. Qiu, G. Zhu, *Angew. Chem. Int. Ed.* 2009, **48**, 9457-9460.
40. G. Zhou, M. Baumgarten, K. Müllen, *J. Am. Chem. Soc.* 2007, **129**, 12211-12221.
41. B. S. Brunschwig, C. Creutz, N. Sutin, *Chem. Soc. Rev.* 2002, **31**, 168-184.
42. N. S. Hush, *Prog. Inorg. Chem.* 1967, **8**, 391-444.
43. D. M. D'Alessandro, F. R. Keene, *Chem. Soc. Rev.* 2006, **35**, 424-440.
44. M. B. Robin, P. Day, *Adv. Inorg. Chem. Radiochem.* 1967, **10**, 247-403.
45. K. D. Demadis, C. M. Hartshorn, T. J. Meyer, *Chem. Rev.* 2001, **101**, 2655-2685.
46. S. Bamberger, D. Hellwinkel, F. A. Neugebauer, *Chem. Ber.* 1975, **108**, 2416-2421.
47. S. Barlow, C. Risko, S.-J. Chung, N. M. Tucker, V. Coropceanu, S. C. Jones, Z. Levi, J.-L. Brédas, S. R. Marder, *J. Am. Chem. Soc.* 2005, **127**, 16900-16911.
48. A.-H. Lu, G.-P. Hao, *Annu. Rep. Prog. Chem., Sect. A:Inorg. Chem.*, 2013, **109**, 484-503.
49. S.-i. Noro, Y. Hijikata, M. Inukai, T. Fukushima, S. Horike, M. Higuchi, S. Kitagawa, T. Akutagawa, T. Nakamura, *Inorg. Chem.* 2013, **52**, 280-285.
50. D. M. D'Alessandro, J. R. R. Kanga, J. S. Caddy, *Aust. J. Chem.* 2011, **64**, 718-722.
51. P. M. Usov, C. Fabian, D. M. D'Alessandro, *Chem. Commun.* **2012**, 48, 3945-3947.
52. M. Nagata, H. Yahiro, M. Shiotani, M. Lindgren, A. Lund, *Chem. Phys. Lett.* **1996**, 256, 27-32.
53. S. Grimme, *J. Comput. Chem.* **2006**, 27, 1787-1799.
54. Kresse, G.; Furthmüller, J. *Comput. Mater. Sci.* **1996**, 6, 15-50.
55. Kresse, G.; Hafner, J. *Phys. Rev. B* **1993**, 48, 13115-13118.



254x190mm (96 x 96 DPI)